Application of a whole-body pharmacokinetic model for targeted radionuclide therapy to NM404 and FLT

2012 Phys. Med. Biol. 57 1641

(http://iopscience.iop.org/0031-9155/57/6/1641)

Phys. Med. Biol. **57** (2012) 1641–1657 doi:10.1088/0031-9155/57/6/1641

Application of a whole-body pharmacokinetic model for targeted radionuclide therapy to NM404 and FLT

Joseph J Grudzinski[1], John M Floberg[1], Sarah R Mudd[2], Justin J Jeffery[3], Eric T Peterson[1], Alice Nomura[4], Ronald R Burnette[2], Wolfgang A Tomé[1,5], Jamey P Weichert[6] and Robert Jeraj[1,6]

[1] Department of Medical Physics, University of Wisconsin School of Medicine and Public Health, 1111 Highland Ave, Madison, WI 53705, USA
[2] Department of Pharmaceutical Sciences, University of Wisconsin School of Pharmacy, 777 Highland Ave, Madison, WI 53705, USA
[3] Arizona Cancer Center, University of Arizona, 1515 N Campbell Ave, Tucson, AZ 85724, USA
[4] Department of Medicine, University of Wisconsin School of Medicine and Public Health, 750 Highland Ave, Madison, WI 53705, USA
[5] Department of Human Oncology, University of Wisconsin School of Medicine and Public Health, 1111 Highland Ave, Madison, WI 53705, USA
[6] Department of Radiology, University of Wisconsin School of Medicine and Public Health, 1111 Highland Ave, Madison, WI 53705, USA

E-mail: grudzinski@wisc.edu

Received 4 October 2011, in final form 10 January 2012
Published 7 March 2012
Online at stacks.iop.org/PMB/57/1641

Abstract

We have previously developed a model that provides relative dosimetry estimates for targeted radionuclide therapy (TRT) agents. The whole-body and tumor pharmacokinetic (PK) parameters of this model can be noninvasively measured with molecular imaging, providing a means of comparing potential TRT agents. Parameter sensitivities and noise will affect the accuracy and precision of the estimated PK values and hence dosimetry estimates. The aim of this work is to apply a PK model for TRT to two agents with different magnitudes of clearance rates, NM404 and FLT, explore parameter sensitivity with respect to time and investigate the effect of noise on parameter precision and accuracy. Twenty-three tumor bearing mice were injected with a 'slow-clearing' agent, ^{124}I-NM404 ($n = 10$), or a 'fast-clearing' agent, ^{18}F-FLT (3′-deoxy-3′-fluorothymidine) ($n = 13$) and imaged via micro-PET/CT pseudo-dynamically or dynamically, respectively. Regions of interest were drawn within the heart and tumor to create time-concentration curves for blood pool and tumor. PK analysis was performed to estimate the mean and standard error of the central compartment efflux-to-influx ratio (k_{12}/k_{21}), central elimination rate constant (k_{el}), and tumor influx-to-efflux ratio (k_{34}/k_{43}), as well as the mean and standard deviation of the dosimetry estimates. NM404 and FLT parameter estimation results were used to analyze model accuracy and parameter sensitivity. The accuracy of the experimental sampling schedule

was compared to that of an optimal sampling schedule found using Cramer–Rao lower bounds theory. Accuracy was assessed using correlation coefficient, bias and standard error of the estimate normalized to the mean (SEE/mean). The PK parameter estimation of NM404 yielded a central clearance, k_{el} (0.009 $\pm$ 0.003 h^{-1}), normal body retention, k_{12}/k_{21} (0.69 $\pm$ 0.16), tumor retention, k_{34}/k_{43} (1.44 $\pm$ 0.46) and predicted dosimetry, D_{tumor} (3.47 $\pm$ 1.24 Gy). The PK parameter estimation of FLT yielded a central elimination rate constant, k_{el} (0.050 $\pm$ 0.025 min^{-1}), normal body retention, k_{12}/k_{21} (2.21 $\pm$ 0.62) and tumor retention, k_{34}/k_{43} (0.65 $\pm$ 0.17), and predicted dosimetry, D_{tumor} (0.61 $\pm$ 0.20 Gy). Compared to experimental sampling, optimal sampling decreases the dosimetry bias and SEE/mean for NM404; however, it increases bias and decreases SEE/mean for FLT. For both NM404 and FLT, central compartment efflux rate constant, k_{12}, and central compartment influx rate constant, k_{21}, possess mirroring sensitivities at relatively early time points. The instantaneous concentration in the blood, C_0, was most sensitive at early time points; central elimination, k_{el}, and tumor efflux, k_{43}, are most sensitive at later time points. A PK model for TRT was applied to both a slow-clearing, NM404, and a fast-clearing, FLT, agents in a xenograft murine model. NM404 possesses more favorable PK values according to the PK TRT model. The precise and accurate measurement of k_{12}, k_{21}, k_{el}, k_{34} and k_{43} will translate into improved and precise dosimetry estimations. This work will guide the future use of this PK model for assessing the relative effectiveness of potential TRT agents.

(Some figures may appear in colour only in the online journal)

Introduction

We have previously introduced a general pharmacokinetic (PK) model for targeted radionuclide therapy (TRT) that predicts the relative effectiveness of potential agents and provides a means of comparing them (Grudzinski *et al* 2010). Molecular imaging is a powerful tool to noninvasively determine the PK parameters; however, it possesses innate sources of error that may make accurate and precise estimation of PK parameters difficult. In particular, noise and parameter sensitivity will affect the accuracy and precision of PK parameters and ultimately the predictive power of a model.

PK model analysis is required to determine how noise and parameter sensitivity will affect parameter estimation. For example, Muzi *et al* demonstrated the impact of noise on the accuracy and precision of measured parameters in FLT studies and investigated the sensitivity of their kinetic model for FLT (Muzi *et al* 2005a). The nature of our model will determine how noise and parameter sensitivity will affect the accuracy and precision of the estimated PK values necessary to predict TRT relative effectiveness.

Since PK parameters have been reported only for a few TRT agents, we aim to determine the PK parameters necessary for our TRT model of two agents of interest whose clearance rates differ by an order of magnitude. Moreover, we aim to investigate the effect of noise on parameter precision and accuracy and explore parameter sensitivity with respect to time. These analyses will assess how accurately and precisely one can predict the relative effectiveness of potential TRT agents using the presented PK model.

Materials and methods

Parameter estimation

NM404: a slow clearing TRT agent. Radioiodinated NM404 is a small molecular phospholipid ether analog that has displayed striking tumor uptake and prolonged tumor retention in over 45 spontaneous and xenograft tumor models (Pinchuk *et al* 2006). Preclinical results strongly suggest that the agent is selectively taken up and retained in both primary and metastatic malignant tumors but not in benign or inflammatory lesions. This gives it great potential as an effective TRT agent when it is radiolabeled with ^{131}I. NM404 can also be radiolabeled with ^{124}I ($t_{1/2,\,\mathrm{phys}} = 100.22$ h; $t_{1/2,\,\mathrm{bio}} \sim 100$ h) and imaged with ^{124}I-PET (Weichert *et al* 2005). Thus, NM404 is an example of a diapeutic molecule that assumes either diagnostic or therapeutic functions depending on the iodine isotope with which it is radiolabeled. The diapeutic nature of the molecule makes it possible to noninvasively derive the necessary PK parameters using ^{124}I PET to predict the relative effectiveness of ^{131}I-NM404 therapy. In this work, it will be used as an example of a TRT agent that is slowly taken up into a tumor and is slowly cleared from the blood.

Synthesis of 18-(p-iodophenyl)octadecyl phosphocholine (NM404) is accomplished via previously reported methodology (Pinchuk *et al* 2006). Radioiodination with ^{124}I (IBA, Belgium) is routinely achieved in 70% isolated radiochemical yield by an isotope exchange reaction (Mangner *et al* 1982). This procedure is currently approved in our existing physician-sponsored University of Wisconsin NM404 IND. Following purification (>99% pure) and accurate mass quantification by HPLC, the radiopharmaceutical is dissolved in absolute ethanol (50–500 ml) and Tween-20 (0.1 ml mg^{-1} of compound). The ethanol is removed under vacuum and the residue is dissolved in sterile water to give a final solution containing no more than 0.4% Tween-20. Sterilization is achieved by filtration through a sterile 0.2 mm filter unit. Injection solutions are tested for pyrogens using the Limulus Amebocyte Lysate test kit. This is the same procedure employed for the preparation, purification and sterile formulation of ^{131}I-labeled NM404 for past patient safety and PK studies.

FLT: a fast clearing TRT agent. 3′-deoxy-3′-fluorothymidine (FLT) was originally a chemotherapy agent used to treat human immunodeficiency virus (Sundseth *et al* 1996). Because FLT correlates with thymidine kinase I expression, it is used as a means to measure cellular proliferation found within malignancies (Viertl *et al* 2010, Brockenbrough *et al* 2011). Clinically, it has been used extensively for diagnosis and grading (Dittmann *et al* 2003, Choi *et al* 2005). Furthermore, a kinetic model has been developed and validated for this agent in lung cancer patients that can be used for treatment response assessment (Muzi *et al* 2005a, 2005b). FLT was used in our work as an example of a tumor-targeting agent that is taken up relatively quickly within a tumor and is cleared quickly from the blood.

^{18}F-FLT was prepared as described by Martin *et al* (2002), modified for synthesis on a Scansys (Denmark) radiochemistry module. Firstly, 1.5 ml ^{18}O H_2O was irradiated with 16.4 MeV protons to produce aqueous ^{18}F ($t_{1/2}$ / 109.7 min; $t_{1/2,\,\mathrm{bio}} \sim 100$ min)—on a PETtrace cyclotron (General Electric). Quaternary Ammonium (Waters, Massachusetts) cartridges trapped >95% of produced activity prior to elution with 500 uL 1 N K_2CO_3 and Kryptofix K2,2,2 in 80/20 MeCN/H_2O. This mixture was azeotropically dried at 110 °C under argon flow to remove residual water and reacted with 10 mg of 3-N-Boc-1-[5-O-(4,40-dimethoxytrityl)-3-O-nosyl-2-deoxy-b-D-lyxofuranosyl]thymine (ABX, Germany) for 15 min at 140 °C in a closed vessel before a 2 min deprotection with 0.5 mL 1N HCl at 110 °C. After cooling, 1.0 mL of 2N sodium acetate neutralized the solution. The product was diluted in

50 mL water and loaded onto a C18 cartridge (Waters, Massachusetts) to remove unreacted fluoride and side-channel reaction impurities. ^{18}F-FLT was then purified by reverse-phase HPLC (Alltech Econosil C18 10 $\times$ 250 mm, 6 ml min^{-1} 90/10 water/EtOH, RT = 700 $\pm$ 15 s). After collection, product ^{18}F-FLT was made isotonic with saline and sterilized by a 22 um filter. Average decay-corrected yields are 16% $\pm$ 5% with specific activities of 4.1 $\pm$ 1.1 Ci/umol.

Animal preparation. Twenty-three nude mice, purchased from Harlan (Madison, WI), were inoculated subcutaneously with 1 $\times$ 10^6 human colon adenocarcinoma LS180 tumor cells suspended in PBS. The mice were housed under standard animal protocol conditions (temperature range, humidity range, 12 h light-dark cycle) and the experiment was warranted and adhered by an animal use protocol created and approved by the University of Wisconsin, Madison, animal use committee.

Ten mice were injected with ^{124}I-NM404 when their tumors reached volumes between 13 and 770 mm^3 (7–14 days) and 13 mice were injected with ^{18}F-FLT when their tumors reached volumes between 146 and 800 mm^3 (4–14 days). To ensure a clean bolus injection, the tail vein was catheterized. Catheters were made using a 30 gauge needle, with the hub removed, attached to PE-1 tubing (Scientific Commodities, Lake Havasu, AZ). The line was filled with heparin whereby a small dose was given prior to injection. After injecting 80–230 μCi of ^{124}I-NM404 or 145–260 μCi of ^{18}F-FLT, the catheter was flushed with 100–150 μL normal saline.

Data acquisition. All mice were imaged on the Inveon micro-PET/CT (Siemens, Knoxville, TN) and anesthetized with 2% isoflurane during scanning. Mice injected with ^{124}I- NM404 were scanned 1, 6, 12, 24, 36, 48, 60, 72, 96, 120, 168 and 240 h post-injection. Each static PET acquisition was composed of 30–40 million counts. The resulting PET images were reconstructed from the three-dimensional (3D) acquisitions using ordered-subset expectation maximization (OSEM) of three dimensions followed by the maximum *a posteriori* algorithm (matrix size = [128128159], pixel size = [0.861, 0.861, 0.796] mm, iterations = 18, subsets = 16 and beta smoothing factor = 0), which provides superior quantitative accuracy for ^{124}I acquisitions because of its noise suppression and increased recovery coefficient with respect to FBP and OSEM2D (Disselhorst *et al* 2010).

Mice injected with ^{18}F-FLT were first CT scanned and then continuously PET scanned for 60 min post-injection. The data were temporally averaged into frames of 6 $\times$ 30, 7 $\times$ 60, 4 $\times$ 300, and 3 $\times$ 600 (frames by seconds). Each frame was reconstructed using the same algorithm that was used for ^{124}I so that a comparison between the agents can be made without introducing any bias. A transformation matrix was applied to both the NM404 and FLT data to ensure PET/CT co-registration and the CT data were used for both scatter and attenuation correction.

A PK model for TRT. Figure 1 is a schematic diagram of the proposed PK model for assessing the relative effectiveness of TRT agents (Grudzinski *et al* 2010). The equations for the change in concentration of radioactivity for both normal body and tumor are

$$\begin{aligned}
\frac{dC_1}{dt} &= k_{21}C_2 - (k_{12} + k_{el} + \lambda)C_1, \\
\frac{dC_2}{dt} &= k_{12}C_1 - (k_{21} + \lambda)C_2, \\
\frac{dC_4}{dt} &= k_{34}C_1(t) - (k_{43} + \lambda)C_4,
\end{aligned} \tag{1}$$

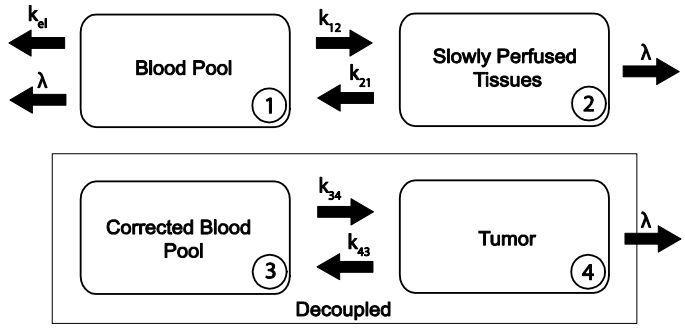

Figure 1. Pharmacokinetic model—a schematic representation of our PK model for TRT agents. The body is desrcibed by a two-compartment model that is decoupled from the tumor compartment. C_1 is the concentration in the blood pool (1), C_2 is the concentration in the slowly perfused tissues (2), and C_4 is the concentration in the tumor (4). The concentration in compartment 1 over time, $C_1(t)$, becomes the forcing (input) function for the tumor. The units for the transfer constants, k_{12}, k_{21}, k_{34} and k_{43} are h^{-1}.

where C_1 is the concentration in the blood pool, C_2 is the concentration in the slowly perfused tissues (skin, fat, muscle, bone and bone marrow) and C_4 is the concentration in the tumor. The units for the transfer rate constants, k_{12}, k_{21}, k_{34} and k_{43} are h^{-1}. λ is the physical decay constant with units of h^{-1}. The corrected blood pool compartment, C_3, is the forcing function used for the tumor compartment which is the fit of the experimentally measured C_1 to the model.

To find the transfer rate constants in equation (1), PK analysis was performed. The PET data were decay corrected so that only biological clearance was considered. Regions of interest (ROIs) were drawn on the PET data within the heart and tumor using the CT data for reference to measure the time-concentration curves (TCCs) of C_1 and C_4. The nature of our model allows us to estimate all of the PK parameters using these two measurements (C_1 and C_4). To measure C_1, an ROI was drawn within the left ventricle as to only encompass blood and attempt to avoid spillover and partial volume effects from the heart wall. C_0 is the instantaneous concentration within the left ventricle after injection. As derived previously (Grudzinski *et al* 2010), the TCC for C_1 can be described by

$$C_1(t) = C_0 \cdot \frac{(\alpha - k_{21})}{(\alpha - \beta)} \cdot \exp(-\alpha \cdot t) + C_0 \cdot \frac{(k_{21} - \beta)}{(\alpha - \beta)} \cdot \exp(-\beta \cdot t). \tag{2}$$

The equation for $C_1(t)$ was simplified into a bi-exponential function defined by

$$C_1(t) = A \cdot \exp(-\alpha \cdot t) + B \cdot \exp(-\beta \cdot t). \tag{3}$$

C_1 was fit to equation (3) using Levenberg–Marquardt nonlinear least-squares optimization (Levenberg 1944, Marquardt 1963, Gavin 2010), implemented in Matlab. Equation (4) was used to derive the micro-rate constants of C_1:

$$\begin{aligned} k_{21} &= \alpha - \frac{A(\alpha - \beta)}{C_0}, \\ k_{21} &= \frac{B(\alpha - \beta)}{C_0} + \beta, \\ k_{\mathrm{el}} &= \alpha + \beta - k_{21} - k_{12}. \end{aligned} \tag{4}$$

By fixing k_{21}, α, β and C_0, $C_{\mathrm{tumor}}(t)$ was fit to equation (5) to determine the tumor-specific micro-rate constants, k_{34} and k_{43}. α and β are macro-rate constants between compartments 1

and 2:

$$C_{\text{tumor}}(t) = C_0 \cdot k_{34}\left[\frac{(k_{21}-k_{43})}{(\alpha-k_{43})(\beta-k_{43})}\exp(-k_{43}\cdot t) + \frac{(k_{21}-\alpha)}{(\beta-\alpha)(k_{43}-\alpha)} \times \exp(-\alpha\cdot t) + \frac{(k_{21}-\beta)}{(k_{43}-\beta)(\alpha-\beta)}\exp(-\beta\cdot t)\right]. \tag{5}$$

k_{43} and k_{34}, the only free parameters in this optimization, are used in conjunction with k_{12}, k_{21} and k_{el} to predict the relative effectiveness of TRT agents on the basis of the tumor absorbed dose (Grudzinski *et al* 2010). Equation (6) describes the relationship between the PK parameters and absorbed dose to the tumor, D_{tumor}, predicted by the model:

$$D_{\text{tumor}} = D_{\text{thresh}}\left[\frac{k_{34}}{k_{43}}\left(\frac{1}{w_1 + w_2\left(\frac{k_{12}}{k_{21}}\right)}\right)\right] \tag{6}$$

where D_{thresh} is the total body dose threshold, and w_1 and w_2 are the proportion of the body encompassed by C_1 and C_2, respectively. This comparative model assumes that each potential agent is radiolabeled with the same long-lived beta-emitting radionuclide and focuses solely on PK properties. The derivation of the model is shown in the appendix. The effect of the long-lived radionuclide on the model is further explained.

Scope and limitations. Early measurement of PK parameters of TRT agents may help predict relative effectiveness, which provides means to expedited agent development or rejection. Our relatively simple model could be used as an initial comparative evaluation of potential TRT agents. The comparative nature of our model requires a common dose-limiting organ by which agents can be compared. Because whole-body dose is often assumed to be a surrogate for bone marrow dose and bone marrow dose is often the dose-limiting organ for TRT agents (Lassmann *et al* 2005), our model uses the whole body to be dose limiting. Some agents, like FLT, will of course be limited by doses to specific organs, particularly clearance organs such as the bladder and liver. While our model does not explicitly account for these dose-limiting organs, the limiting effect of clearance on these organs is in part accounted for the k_{12}/k_{21} term in equation (6). Promising TRT agents would require agent specific evaluation to determine organ and tumor doses. Once a potential TRT agent shows relative effectiveness via our model, 3D dosimetric calculations can be performed.

Another limitation of this model is that it assumes all tissue to be homogeneous media. Variations in atomic number within the body may influence the distribution of dose delivered by low-energy photons. For example, interfaces between soft tissues, air and bone have the potential to create inhomogeneous dose distributions. Furthermore, by only considering self-dose within a compartment (radiation from beta particles), we have neglected cross-dose amongst compartments (radiation from gamma rays) which ultimately reduces the radiation dose absorbed by a compartment. Because of these limitations, the proposed model is not meant to provide absolute quantification of TRT radiation dosimetry. However, the model's general nature could make it a valuable comparative tool.

Propagation of error. Levenberg–Marquardt optimization allows for the determination of both the asymptotic standard error of each parameter and the standard error of the fit (Gavin 2010). Uncertainty in the data caused by variability in ROI definition, biological processes and the lack of counts within the ROI, translates into uncertainty in the dosimetry. The summation of these uncertainties were represented by a Gaussian probability density functions (PDFs) at each data point and then propagated through the model by the fitting process. This leads to PDFs for each PK parameter that ultimately create Gaussian PDFs for D_{tumor}. Using Monte Carlo analysis, 1000 combinations of parameters were randomly sampled around a PDF with

Table 1. Parameter values for NM404 within an LS180 xenograft model

Parameter (units)	Mean value	Range for optimization
C_0 (%ID ml^{-1})	15	11–21
k_{12} (h^{-1})	0.13	0.05–0.27
k_{21} (h^{-1})	0.14	0.14–0.25
k_{el} (h^{-1})	0.02	0.007–0.044
k_{34} (h^{-1})	0.03	0.023–0.061
k_{43} (h^{-1})	0.02	0.007–0.027

Table 2. Parameter values for FLT within an LS180 xenograft model.

Parameter (units)	Mean value	Range for optimization
C_0 (%ID ml^{-1})	18	11–36
k_{12} (min^{-1})	0.39	0.17–0.71
k_{21} (min^{-1})	0.21	0.073–0.29
k_{el} (min^{-1})	0.02	0.011–0.071
k_{34} (min^{-1})	0.03	0.013–0.034
k_{43} (min^{-1})	0.02	0.027–0.070

a width equal to the standard error and a center equal to the mean value of the PK parameters. Equation (6) was used to compute D_{tumor} for each combination, respectively. The standard deviation of D_{tumor} was used to represent the uncertainty in dosimetry for each dataset.

Model analysis. The proposed PK model was evaluated to determine the extent to which the information obtained from a typical imaging study is sufficient to produce a unique solution with parameters that are both accurately and precisely measured. The model was characterized with respect to parameter sensitivity and susceptibility to noise to establish the most reliable approach for parameter estimation.

Sensitivity analysis. A sensitivity analysis was performed on the proposed PK model to measure the degree to which a change in an individual input parameter results in a change in the output of the model. Parameters with high sensitivity are more likely to be estimated accurately than those with lower sensitivity because noise will have a great affect. Parameters with similar sensitivity functions could be difficult to estimate independently. The sensitivity equation, shown in equation (7), represents the fractional change in the total TCC at a given time, t, after injection as a result of a small change in the parameter (δk_α) (Bassingthwaighte and Chaloupka 1984):

$$\text{Sensitivity}_{k_\alpha}(t) = \frac{\mathrm{d}\,\text{TCC}(t)/\text{TCC}(t)}{\mathrm{d}k_\alpha/k_\alpha}. \tag{7}$$

Sensitivity analyses were performed according to the average parameter values for NM404 and FLT, which are shown in tables 1 and 2, respectively. The sensitivity of each parameter was derived by analytically differentiating the equation for each curve. The operating point, k_α, was set at the mean PK values for NM404 and FLT.

Optimal sampling. Because PK parameters are sensitive at different time points, temporal sampling has a great effect on the accuracy and precision of parameter estimation. Therefore, optimal sampling strategies could improve accuracy of parameter estimation, and several such strategies have been described in the literature (Li *et al* 2001, Cercignani and Alexander 2006, Xie *et al* 2008). In addition, optimal sampling can reduce cost and patient discomfort associated with multiple imaging sessions if the model is expanded into human use.

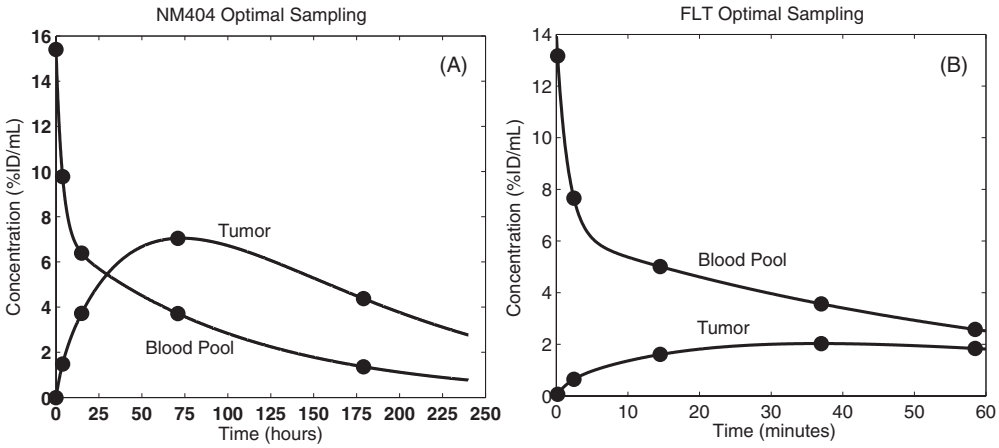

Figure 2. Optimal sampling schedules: (A) NM404 – 0, 3.86, 14.88, 71 and 179 h. (B) FLT - 0, 2.44, 14.50, 37 and 58.50 min post-injection.

The effects of temporal sampling on parameter estimates were evaluated using the theory of Cramer–Rao lower bounds (CRLB). CRLB finds the optimal sampling points that minimize the maximum prediction variance of the PK parameters while maximizing precision of parameter estimates (Li *et al* 2001). CRLB was implemented in Matlab to derive the optimal sampling schedules for NM404 and FLT given the estimated PK parameter values obtained from the FLT and NM404 experiments. The latest time points considered in the optimization were 240 h and 60 min post-injection for NM404 and FLT, respectively. Objective functions were created based on CRLB to optimize sampling for multiple parameters simultaneously. The optimal sampling schedules for NM404 and FLT are shown in figure 2.

Noise simulations. To investigate the model's ability to accurately estimate the key PK parameters of NM404 and FLT across their expected preclinical range, it was necessary to use realistic standardized data. A set of 250 noisy simulated TCCs were generated for C_1 and C_4 according to both experimental and optimal sampling schedules and the values found in tables 1 and 2, respectively. Poisson noise was added to each simulated TCC, scaled to the total counts and the duration of each time frame according to equation (8):

$$\sigma_{n,i} = c\sqrt{f_{n,i}d_i/t_i^{\mathrm{dur}}}, \tag{8}$$

where $f_{n,i}$ is the activity concentration in the nth image ROI and at the ith scan after decay and scan-duration correction, $d_i = \exp(\lambda t_i)$ is the isotope decay correction factor, with λ the decay constant and t_i the acquisition time at the ith scan, t_i^{dur} is the scan duration at the ith scan, and c is a constant which scales the Gaussian noise with standard deviation close to the pre-clinical situation (Wang *et al* 2009). For the NM404 and FLT investigations, c was set to 2% and 7.5%, respectively, as to replicate the Gaussian noise seen in imaging studies, while the other variables of equation (8) were set to the NM404 and FLT experimental or optimal sampling parameters.

For both the experimental and optimal sampling schedules, the true (simulated input) and estimated parameter values were compared by examining the correlation coefficient for estimated versus true parameter, the percentage bias (the difference in the measurements for estimated versus true parameter) and the precision (standard error of the estimate for the estimated versus true parameter divided by the mean true parameter, SEE/mean).

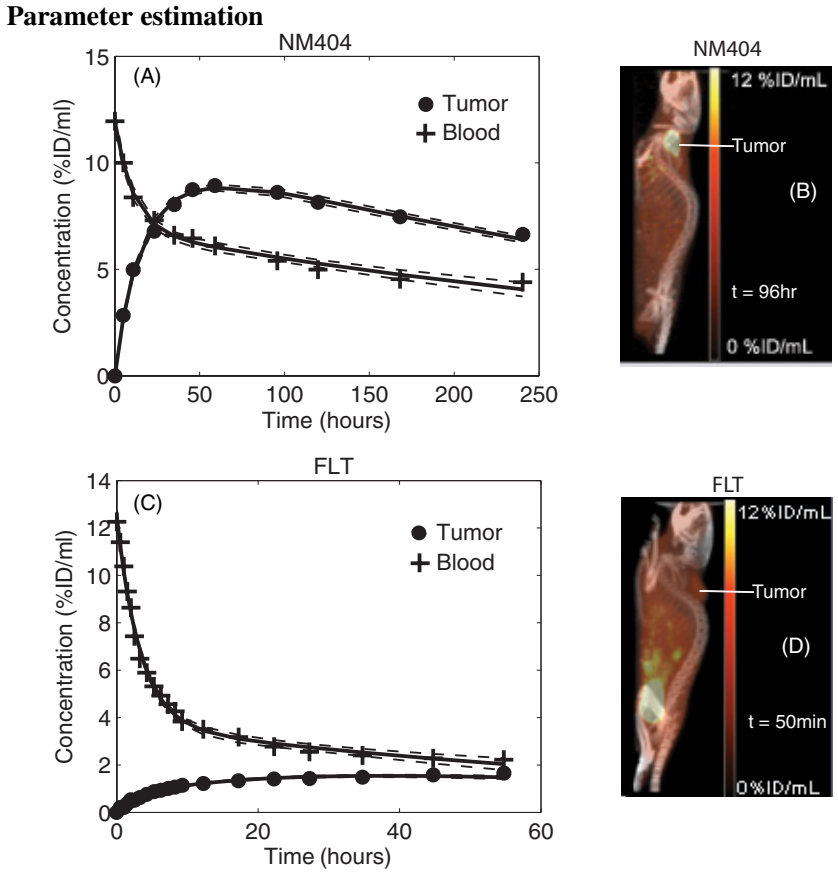

Figure 3. Representative data from the experiment—the concentration (%ID ml^{-1}) of NM404 and FLT in the tumor and blood over time are shown in (A) and (C), respectively. The dotted lines represent 95% confidence intervals for curve-fitting. Example PET/CT data sets are shown for NM404 and FLT in (B) and (D), respectively.

Results

Parameter estimation

Representative TCC and PET/CT data for NM404 and FLT are shown in figure 3. Note how the differences in peak tumor uptake in (A) and (C) of figure 3 are reflected in the differences in tumor signal intensities within the PET/CT data of (B) and (D) of figure 3.

The estimates of the parameters for NM404 from the experimental data are found in figure 4. After estimating k_{12} (0.054 $\pm$ 0.014 h^{-1}), k_{21} (0.079 $\pm$ 0.018 h^{-1}), k_{el} (0.009 $\pm$ 0.003 h^{-1}), k_{34} (0.033 $\pm$ 0.012 h^{-1}) and k_{43} (0.023 $\pm$ 0.005 h^{-1}), D_{tumor} (3.47 $\pm$ 1.24 Gy) was calculated by using equation (6), assuming that $D_{thresh} = 2$ Gy, $w_1 = 0.2$ and $w_2 = 0.8$.

The results of the parameter estimation for FLT from the experimental data are found in figure 5. After deriving k_{12} (0.408 $\pm$ 0.202 min^{-1}), k_{21} (0.176 $\pm$ 0.061 min^{-1}), k_{el} (0.050 $\pm$ 0.025 min^{-1}), k_{34} (0.020 $\pm$ 0.005 min^{-1}) and k_{43} (0.033 $\pm$ 0.012 min^{-1}), D_{tumor} (0.61 $\pm$ 0.20 Gy) was calculated using equation (6), assuming $D_{thresh} = 2$ Gy, $w_1 = 0.2$ and $w_2 = 0.8$.

Figure 6 shows the tumor dosimetry results from the experimental data for FLT and NM404. Note that NM404 yields a greater D_{tumor} than FLT. Figure 7 shows a graphical

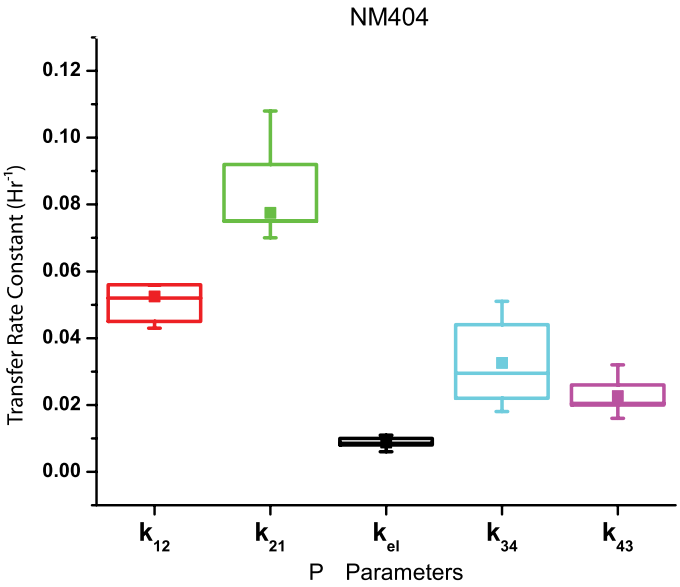

Figure 4. A graphical representation of the results for NM404 parameter estimation—the box plots indicate the range of the means for each for NM404 between 25% and 75% of the median. The mean is also indicated with a solid box.

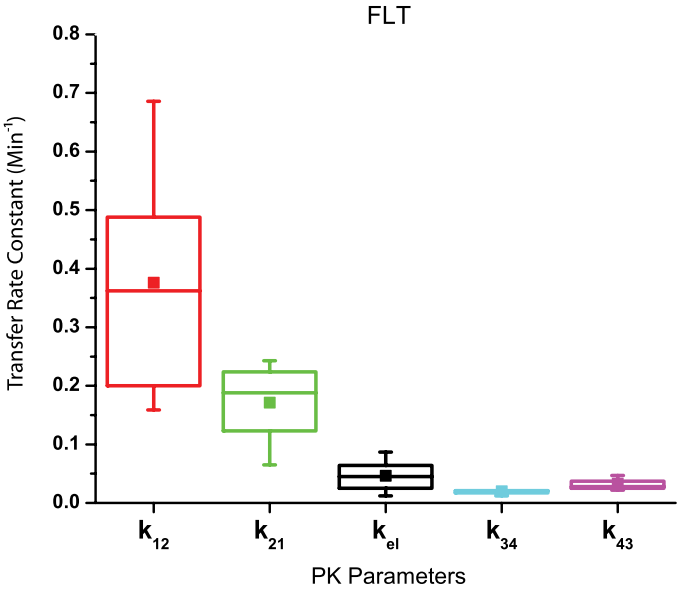

Figure 5. A graphical representation of the results for FLT parameter estimation—the box plots indicate the range of the means for each PK parameter for FLT between 25% and 75% of the median. The mean is also indicated with a solid square.

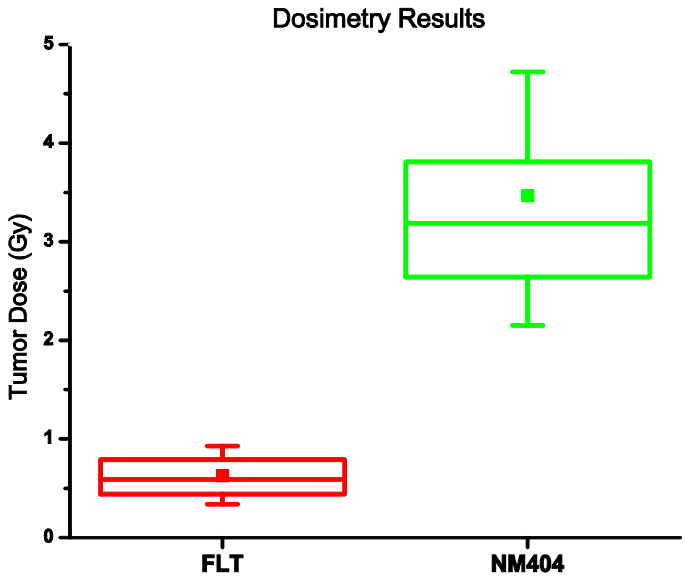

Figure 6. Dosimetry results—the box plots indicate the range of the results from the experiment between 25% and 75% of the median. The mean is also indicated with a solid square.

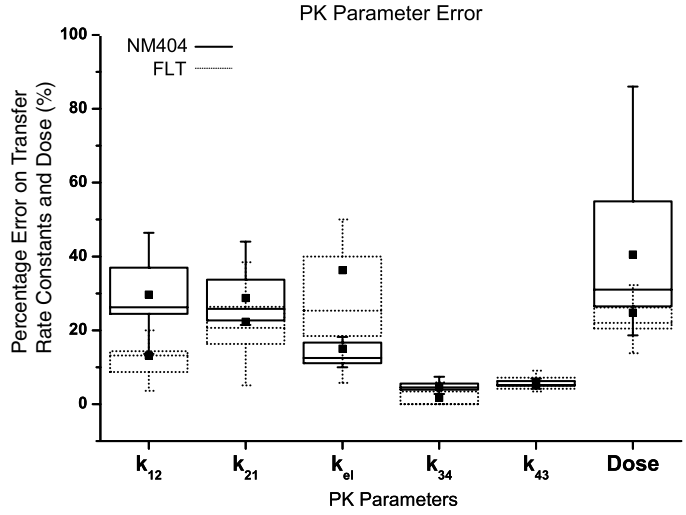

Figure 7. A graphical representation of the parameter per cent error for NM404 and FLT—the standard errors from the parameter estimation for NM404 were converted to the per cent error. The box plots indicate the range of the parameter error for each parameter between 25% and 75% of the median. The mean error is indicated with a solid square. The standard deviation of the dose was taken as the standard deviation of the PDF generated from the Monte Carlo simulations outlined above.

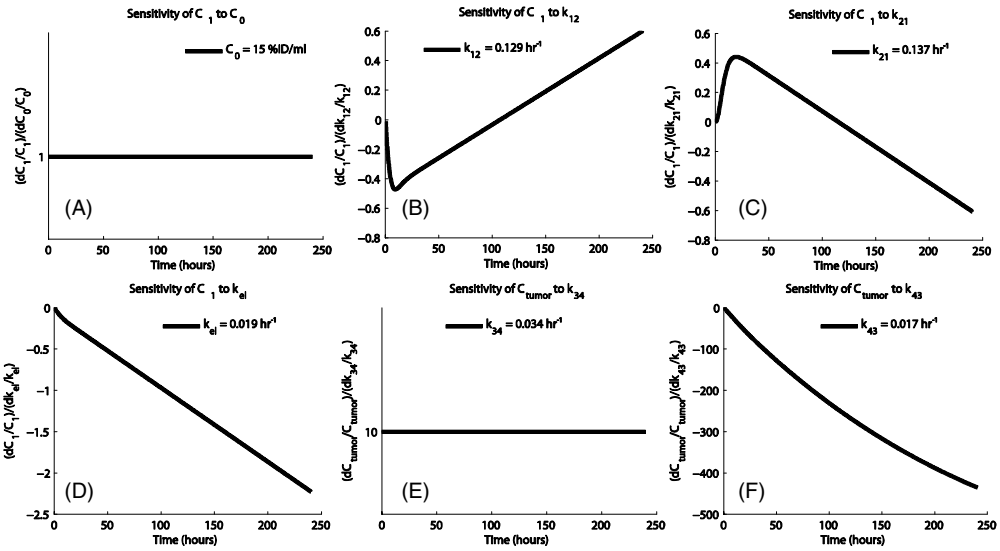

Figure 8. Sensitivity functions of NM404—the sensitivity functions represent the time-dependent change in C_1 and C_{tumor} resulting from a change in the parameter value. Sensitivities are shown for C_0 (A), k_{12} (B), k_{21} (C), k_{el} (D), k_{34} (E) and k_{43} (F).

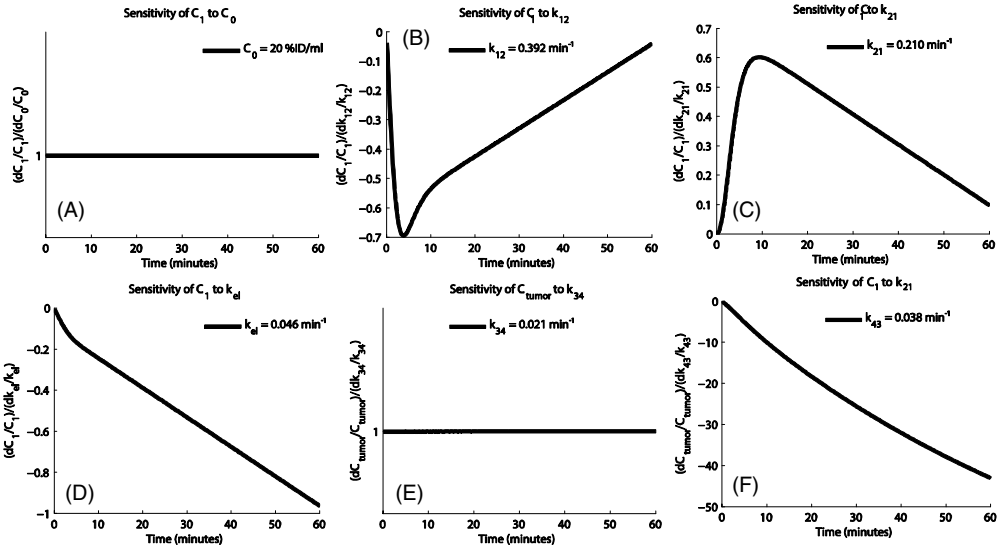

Figure 9. Sensitivity functions of FLT—the sensitivity functions represent the time-dependent change in C_1 and C_{tumor} resulting from a change in the parameter value. Sensitivities are shown for C_0 (A), k_{12} (B), k_{21} (C), k_{el} (D), k_{34} (E) and k_{43} (F).

representation for per cent error of the experimental data for NM404 and FLT. Note that the per cent error in dose is proportional to the per cent error in k_{12} and k_{21}.

Model analysis

Sensitivity analysis. The relative sensitivities of C_1 and C_4 for NM404 and FLT are shown in figures 8 and 9, respectively. The curves show that the sensitivity of C_1 to k_{21} mirrors that of

Table 3. Model accuracy for NM404—the experimental simulations were performed with $c = 2\%$

	Experiment sampling			Optimal sampling			Optimal sampling—last point removed		
Parameter	r	Bias (%)	SEE/mean (%)	r	Bias (%)	SEE/mean (%)	r	Bias (%)	SEE/mean (%)
C_0	0.98	4	5.1	1.0	0	1.4	1.0	0	1.4
k_{12}	0.94	14	23	0.98	−1.3	9	0.98	−0.6	9.5
k_{21}	0.93	9.3	17	0.93	−1.8	15	0.92	−1.3	16
k_{12}/k_{21}	0.99	5.7	8	1.0	0	5.6	0.99	0.1	7.5
k_{el}	1.0	4.8	6.8	1.0	−0.2	3.4	0.99	−0.5	5.2
k_{34}	1.0	−0.6	1.7	0.99	−0.2	2.8	0.99	0.5	3.4
k_{43}	0.97	−1.1	3.3	0.93	−0.2	5.4	0.75	1.7	11.6
D_{tumor}	0.99	−5.0	8.3	0.99	−0.3	5.7	0.99	−1.6	8.6

Table 4. Model accuracy for FLT—the experimental simulations were performed with $c = 7.5\%$

	Experiment sampling			Optimal sampling			Optimal sampling—last point removed		
Parameter	r	Bias (%)	SEE/mean (%)	r	Bias (%)	SEE/mean (%)	r	Bias (%)	SEE/mean (%)
C_0	0.98	0.4	6.0	1.0	1.9	3.4	1.00	2.1	3.4
k_{12}	0.91	−0.7	14	0.97	3.8	9.7	0.97	0.8	8.7
k_{21}	0.94	−1.0	13	0.97	2.7	8.5	0.88	15	24
k_{12}/k_{21}	0.99	0.4	5.5	1.0	1.1	5.2	0.98	−20	31
k_{el}	0.93	0.9	16.5	0.99	4.5	8.0	0.36	66	84
k_{34}	0.99	−0.6	3.5	0.97	−1.3	6.7	0.87	−1.5	14
k_{43}	0.99	−0.8	5.1	0.94	−1.8	11.2	0.63	−2.2	38
D_{tumor}	1.0	−0.5	7.1	1.0	−0.9	6.0	0.07	−351	2746

k_{12} indicating a high degree of overlapping sensitivity. This could cause difficulty in estimating these parameters independently and could be the reason why our data shows uncertainty in the parameter estimation for both NM404 and FLT.

Noise simulations. Tables 3 and 4 compare experimental sampling, optimal sampling and optimal sampling with the last point removed for NM404 and FLT, respectively. The correlation coefficients for estimated versus true parameter values for all parameters are >92% and >90% for NM404 and FLT, respectively, which reflects robust estimates. The parameters with the highest bias and SEE/mean are k_{12}, k_{21} and k_{el} for NM404, and k_{12}, k_{21} and k_{43} for FLT. The uncertainty in these estimations propagates into uncertainty in estimating absorbed dose (D_{tumor}). However, note that the body ratio, k_{12}/k_{21}, has less error than the individual parameters k_{12} and k_{21}.

With optimal sampling, the associated error (SEE/mean) for both k_{12} and k_{21} are decreased which decreases error in D_{tumor}. When the final data point is removed, the errors of k_{43} and k_{el} increase slightly for NM404 but drastically for FLT, which indicates that k_{43} and k_{el} are most sensitive to later sampling points. The error associated with k_{21} also increases drastically for FLT when the last point is removed. This indicates that the final time point is important for maintaining precision for k_{21} as well.

Discussion

The tumor dosimetry results in figure 6 demonstrate that NM404 shows more promise as a potential TRT agent than FLT. NM404 has both higher tumor influx-to-efflux ratios (k_{34}/k_{43}) and lower C_1 efflux-to-influx ratios (k_{12}/k_{21}) compared to FLT, which contributes to higher possible absorbed doses (D_{tumor}). It is advantageous to have a small k_{12}/k_{21} ratio, like NM404 has, because the transfer from the central compartment into the peripheral compartment is slow. Referring to the derivation of the PK model (Grudzinski *et al* 2010), there are two reasons why this is important. Firstly, the peripheral compartment is a majority of the whole body. If the TRT agent remains in the peripheral compartment, including dose-limiting organs, this will lead to lower achievable tumor doses because whole-body dose limits are reached earlier. Secondly, the central compartment TCC becomes the input into the tumor compartment which ultimately transfers the TRT agent into the tumor and increases the delivered dose.

Our propagation of error analysis dictates that noisy C_1 data translate into uncertain k_{12} and k_{21} values, which translate into uncertain dosimetry calculations and model predictions. Figure 7 shows that there is more error in NM404 dose estimates compared to FLT because of larger errors in k_{12} and k_{21} estimates. Besides noise, ROI definition is another source of uncertainty that has the potential to cause error in the PK parameters. Automatic methods of ROI definition would most likely have smaller variances than manual methods due to their exact nature but might suffer from larger biases compared to manual methods.

The noise simulations showed that the parameters with the least precision and accuracy are k_{12} and k_{21}, which can be attributed to overlapping sensitivity functions. However, the precision and accuracy of the ratio k_{12}/k_{21} are relatively good (cf tables 3 and 4). As estimates for D_{tumor} rely on this ratio, they are still very precise and accurate.

Optimal sampling of a TCC takes into account the model sensitivity with respect to time, with the objective of reducing error propagation and improving the precision of parameter estimates. In our noise simulations, optimal sampling helps to make individual C_0, k_{12}, k_{21} and k_{el} estimates more accurate and precise but k_{34} and k_{43} estimates less accurate and precise. This is due to the fact that the latest possible sampling point for the optimal sampling schedule was the latest sampling point in the experimental protocol. Despite the reduced precision in k_{34} and k_{43} estimates, optimal sampling helped improve the precision of estimates for D_{tumor} for both NM404 and FLT.

Optimal sampling can lead to more bias in the estimates. Interestingly, optimal sampling decreased the bias of NM404 but increased the bias for FLT compared to experimental sampling, indicating that the drastic reduction in sampling points for FLT introduces a bias to the estimates. This problem can be alleviated if additional sampling points are added at later time points for FLT.

Removing the last time point is detrimental to the accuracy and precision of the TRT model. If the last point of the optimal sampling schedule is removed, there is an increase in the errors associated with k_{43} and k_{el}. The sensitivity functions in figures 8 and 9 indicate that these parameters are very sensitive to later sampling times, which reiterates the need for later samples to increase the precision of parameter estimation. Because of animal safety issues and decaying tracers, it is often difficult to adequately sample at very late time points and inaccuracy and imprecision are often unavoidable as a result.

Conclusions

We have developed a model that could allow researchers to assess the relative effectiveness of potential TRT agents at the early stages of development. Because the model involves

comparison between agents, it relies on the measurement of PK parameters of TRT agents. In this work, we have for the first time determined the PK parameter values for two real agents, NM404 and FLT. The PK parameters were used to estimate D_{tumor} which is directly related to the relative effectiveness of the agent. The parameter estimation process showed that noisy data within C_1 led to uncertain k_{12} and k_{21} values. Sensitivity analysis showed that the sensitivity functions of k_{12} and k_{21} overlap which could describe their increased uncertainty. In addition, the sensitivity functions of k_{el} and k_{43} showed that their measurement precision can be increased if the data are sampled at later time points. Model analysis showed that optimal sampling via CRLB can improve the accuracy and precision in measuring k_{12} and k_{21}, whereas sampling at later time points can improve the accuracy of k_{el} and k_{43}. The precise and accurate measurement of k_{12}, k_{21}, k_{el}, k_{34} and k_{43} will translate into more accurate and precise D_{tumor} calculations.

Understanding our model can help reduce imaging time points without substantially decreasing parameter precision. Overall, we explored the relevant properties of the model that contribute to its optimal use. Our work demonstrates that relative effectiveness can be estimated accurately and precisely even though individual parameter might not be. We have introduced a PK modeling approach to compare potential TRT agents in relative terms, demonstrated such a comparison with NM404 and FLT and explored the relevant properties of the model.

Acknowledgments

The authors would like to thank the members of the UW Madison Cyclotron Research Group for production of the FLT tracer. The authors would also like to acknowledge financial support from the University of Wisconsin Medical Scientist Training Program, the University of Wisconsin Department of Radiology, and the NIH Radiological Sciences Training grant T32 CA009206.

One of the authors, Jamey Weichert, is the founder of Cellectar (now Novelos Therapeutics) which owns the licensing rights to NM404 and related technologies and therefore has a financial interest in this agent.

Appendix

The tumor compartment within the linear system is assumed not to perturb the two-compartment open model of the body because of its neglible volume compared to the other two body compartments. Therefore, the tumor compartment was decoupled from the normal body compartments. The equations for the change in concentration of radioactivity for both normal body and tumor are found in equation (1).

The units of the inter-compartmental rate constants, $k_{12}, k_{21}, k_{34}, k_{43}, k_{\text{el}}$, and physical decay constant, λ, are h^{-1}. The solution to each equation, solved via Laplace transforms, represents the TCC of each compartment that is used to determine radiation dosimetry. The analytical solutions of radioactivity concentration, $C(t)$, are converted to time activity, $A(t)$, by incorporating the volume of each compartment and A_0, the initial activity within compartment 1. An analytical PK model was derived for each compartment:

$$A_1(t) = V_1 \cdot \frac{A_0}{V_1}\left[\frac{(\zeta-\alpha)\exp(-\alpha t) - (\zeta-\beta)\exp(-\beta t)}{(\beta-\alpha)}\right],$$

$$A_2(t) = V_2 \cdot \frac{A_0 \cdot k_{12}}{V_1}\left[\frac{\exp(-\alpha t) - \exp(-\beta t)}{(\beta-\alpha)}\right],$$

$$A_4(t) = V_4 \cdot \frac{A_0 \cdot k_{34}}{V_1}\left[\frac{(\zeta-\sigma)}{(\alpha-\sigma)(\beta-\sigma)}\exp(-\sigma t) + \frac{(\zeta-\alpha)}{(\beta-\alpha)(\sigma-\alpha)}\exp(-\alpha t) + \frac{(\zeta-\beta)}{(\sigma-\beta)(\alpha-\beta)}\exp(-\beta t)\right], \tag{A.1}$$

where A_0 is injected activity, $\zeta = k_{21} + \lambda,\ \sigma = k_{43} + \lambda,\ \gamma = k_{12} + k_{el} + \lambda,$

$$\alpha = \tfrac{1}{2}[(\gamma+\zeta) + \sqrt{(\gamma+\zeta)^2 - 4(\gamma\zeta - k_{21}k_{12})}],$$
$$\beta = \tfrac{1}{2}[(\gamma+\zeta) - \sqrt{(\gamma+\zeta)^2 - 4(\gamma\zeta - k_{21}k_{12})}]. \tag{A.2}$$

The analytical PK model was adapted into a TRT model by relating whole-body dose threshold, D_{thresh}, to tumor dose, D_{tumor}, via specific PK parameters of each compartment. w_1 and w_2 are the proportion of the total body volume of each body compartment, respectively:

$$D_{tumor} = D_{thresh}\left[\frac{k_{34}}{k_{43}}\left(\frac{1}{w_1 + w_2\left(\frac{k_{12}}{k_{21}}\right)}\right) + \lambda\frac{k_{34}}{k_{43}}((k_{43}-k_{21})(w_1k_{21} + w_2k_{12}) - w_1k_{21})\right]. \tag{A.3}$$

The complete derivation of equation (A.3) is found in the appendix of Grudzinski *et al* (2010). Our model assumes bone marrow to be the dose-limiting organ. Because whole-body dose is a surrogate for bone marrow dose, the whole-body dose threshold, D_{thresh}, is set according to a bone marrow limit of 2 Gy (Lassmann *et al* 2005). Our model also assumes homogeneous uptake within each compartment, homogeneous dose deposition and homogeneous tissue within each compartment. Lastly, each compartment only experiences self-dose, and neighboring dose deposition is neglected.

The targeting agent was assumed to be radiolabeled with a long-lived beta-emitting radionuclide such as ^{131}I ($\lambda = 0.003\,61\ h^{-1}$) or ^{90}Y ($\lambda = 0.0108\ h^{-1}$). This physical decay is reflected by λ in equation (1). Because the decay constant for most TRT radionuclides is very small, the second part of the equation (A.3) is negligible and the equation becomes

$$D_{tumor} = D_{thresh}\left[\frac{k_{34}}{k_{43}}\left(\frac{1}{w_1 + w_2\left(\frac{k_{12}}{k_{21}}\right)}\right)\right]. \tag{A.4}$$

References

Bassingthwaighte J B and Chaloupka M 1984 Sensitivity functions in the estimation of parameters of cellular exchange *Fed. Proc.* **43** 181–4

Brockenbrough J S *et al* 2011 Tumor 3′-deoxy-3′-18F-fluorothymidine (18F-FLT) uptake by PET correlates with thymidine kinase 1 expression: static and kinetic analysis of 18F-FLT PET studies in lung tumors *J. Nucl. Med.* **52** 1181–8

Cercignani M and Alexander D C 2006 Optimal acquisition schemes for *in vivo* quantitative magnetization transfer MRI *Magn. Reson. Med.* **56** 803–10

Choi S J, Kim J S, Kim J H, Oh S J, Lee J G, Kim C J, Ra Y S, Yeo J S, Ryu J S and Moon D H 2005 [18F]3′-deoxy-3′-fluorothymidine PET for the diagnosis and grading of brain tumors *Eur. J. Nucl. Med. Mol. Imaging* **32** 653–9

Disselhorst J A, Brom M, Laverman P, Slump C H, Boerman O C, Oyen W J G, Gotthardt M and Visser E P 2010 Image-quality assessment for several positron emitters using the NEMA NU 4-2008 standards in the siemens Inveon small-animal PET scanner *J. Nucl. Med.* **51** 610–7

Dittmann H, Dohmen B M, Paulsen F, Eichhorn K, Eschmann S M, Horger M, Wehrmann M, Machulla H J and Bares R 2003 [18F]FLT PET for diagnosis and staging of thoracic tumours *Eur. J. Nucl. Med. Mol. Imaging* **30** 1407–12

Gavin H 2010 The Levenberg–Marquardt method for nonlinear least squares curve-fitting problems (Available at http://www.duke.edu/∼hpgavin/ce281/lm.pdf)

Grudzinski J J, Burnette R R, Weichert J P and Jeraj R 2010 Dosimetric effectiveness of targeted radionuclide therapy based on a pharmacokinetic landscape *Cancer Biother. Radiopharm.* **25** 417–26

Lassmann M, Hanscheid H, Reiners C and Thomas S R 2005 Blood and bone m0arrow dosimetry in radioiodine therapy of differentiated thyroid cancer after stimulation with rhTSH *J. Nucl. Med.* **46** 900–1

Levenberg K 1944 A method for the solution of certain non-linear problems in least squares *Q. Appl. Math.* **2** 164–8

Li X, Feng D and Wong K 2001 A general algorithm for optimal sampling schedule design in nuclear medicine imaging *Comput. Methods Programs Biomed.* **65** 45–59

Mangner T J, Wu J L and Wieland D M 1982 Solid-phase exchange radioiodination of aryl iodides. Facilitation by ammonium sulfate *J. Org. Chem.* **47** 1484–8

Marquardt D W 1963 An algorithm for least-squares estimation of nonlinear parameters *SIAM J. Appl. Math.* **11** 431–41

Martin S J, Eisenbarth J A, Wagner-Utermann U, Mier W, Henze M, Pritzkow H, Haberkorn U and Eisenhut M 2002 A new precursor for the radiosynthesis of [18F]FLT *Nucl. Med. Biol.* **29** 263–73

Muzi M, Mankoff D A, Grierson J R, Wells J M, Vesselle H and Krohn K A 2005a Kinetic modeling of 3′-deoxy-3′-fluorothymidine in somatic tumors: mathematical studies *J. Nucl. Med.* **46** 371–80

Muzi M, Vesselle H, Grierson J R, Mankoff D A, Schmidt R A, Peterson L, Wells J M and Krohn K A 2005b Kinetic analysis of 3′-deoxy-3′-fluorothymidine PET studies: validation studies in patients with lung cancer *J. Nucl. Med.* **46** 274–82

Pinchuk A N, Rampy M A, Longino M A, Skinner R W, Gross M D, Weichert J P and Counsell R E 2006 Synthesis and structure-activity relationship effects on the tumor avidity of radioiodinated phospholipid ether analogues *J. Med. Chem.* **49** 2155–65

Sundseth R, Joyner S S, Moore J T, Dornsife R E and Dev I K 1996 The anti-human immunodeficiency virus agent 3′-fluorothymidine induces DNA damage and apoptosis in human lymphoblastoid cells *Antimicrob. Agents Chemother.* **40** 331–5

Viertl D *et al* 2010 Increase of [(18)F]FLT tumor uptake *in vivo* mediated by FdUrd: toward improving cell proliferation positron emission tomography *Mol. Imaging Biol.* **13** 321–31

Weichert J P, Moser A R, Weber S M, Qi C and Longino M A 2005 Radioiodinated NM404-a universal tumor imaging agent? *Acad. Radiol.* **12** S58–9

Xie J, Gallichan D, Gunn R N and Jezzard P 2008 Optimal design of pulsed arterial spin labeling MRI experiments *Magn. Reson. Med.* **59** 826–34

Wang W *et al* 2009 Evaluation of a compartmental model for estimating tumor hypoxia via FMISO dynamic PET imaging *Phys. Med. Biol.* **54** 3083